The sensitivity of converted-phase extended images to P- and S-wavespeed variations

Andrey H. Shabelansky, Earth Resources Laboratory, Massachusetts Institute of Technology; Alison Malcolm, Memorial University of Newfoundland; and Michael Fehler, Earth Resources Laboratory, Massachusetts Institute of Technology*

SUMMARY

Converted-phase (CP) imaging produces high resolution images and can be used effectively for updating both P- and S-wave speed models with an optimization scheme that is formulated in the extended image domain. This optimization is referred to as source-independent converted-phase WEMVA (SICP-WEMVA). However, the convergence of the optimization scheme depends on the selection of parameters and the formulation of the objective functions and their gradients. In this study, we investigate the sensitivity of the extended images for SICP-WEMVA to the domain where the objective function is formulated. We derive analytically the behavior of the seismic energy (i.e., seismic moveout) in the extended horizontal and vertical subsurface space-lag images as a function of P- and S-wave speed variations, and compare them with numerical results. The results of the moveout analysis demonstrate that the extended vertical subsurface space-lag images have higher sensitivity to the background P- and S-wave speed variations than the horizontally extended images and thus may have significant implications on the resolution and convergence of the SICP-WEMVA.

INTRODUCTION

In recent years, full waveform velocity analysis methods have become standard and the use of elastic waves is now drawing more attention. Converted phase (CP) waves are an integrated part of the recorded elastic seismic signal and are investigated in numerous studies in the research areas of VSP data (e.g., Esmersoy, 1990; Stewart, 1991; Xiao and Leaney, 2010), surface reflection (e.g., Purnell, 1992; Stewart et al., 2003; Hardage et al., 2011) and transmission seismic data (e.g., Vinnik, 1977; Vinnik et al., 1983; Bostock et al., 2001; Rondenay et al., 2001; Shang et al., 2012; Brytic et al., 2012; Shabelansky et al., 2014). In particular, e.g., Xiao and Leaney (2010) and Shang et al. (2012) show that converted phase seismic images can be calculated using one elastic wave propagation without using source information (i.e., location, mechanism, time-function), and may have higher resolution and fewer artifacts than reflection type imaging (Shabelansky et al., 2012). Shabelansky et al. (2013, 2015) presented an analysis for updating elastic P and S wave speed models based on the source independent converted phase imaging framework in the so-called extended image gather domain. This analysis is referred to as source-independent converted-phase WEVMA (SICP-WEMVA). For this technique, the misfit function is calculated in the extended image gather domain from the interference between P and converted S (or/and S and converted P) waves, and we call the distribution of this wave interference its moveout. The investigation of the moveout behavior is of a great importance because it shows how errors in P- and S-wave speeds translate to different shaped curves in the extended images, and thus may affect the choice of minimization algorithm and improve the accuracy and convergence of SICP-WEMVA.

In this study we investigate analytically and numerically the behavior of the moveout for SICP-WEMVA as a function of P- and S-wave speed models. The study is divided into two parts. In the first part, we present an analytical derivation of the moveouts in the extended horizontal subsurface space lag image gather domain and compare the analytical with numerically calculated moveouts. In the second part, we conduct the same study in the extended vertical subsurface space lag images and present the advantages of vertical over horizontal extended image gathers.

MOVEOUT DERIVATION FOR SICP-WEMVA

Horizontal subsurface space-lag image gather

We begin our derivation of the moveout for SICP-WEMVA (Shabelansky, 2015) with equations for travel times between a conversion point in the subsurface at (x_0, z_0) and recordings of the P- and S-waves at two receivers at the surface at $(x_p, 0)$ and $(x_s, 0)$ (see Figure 1). The travel time for the P-wave is given as

$$t_p = \frac{d_p}{\alpha_0} = \frac{\sqrt{(x_p - x_0)^2 + z_0^2}}{\alpha_0}, \tag{1}$$

and for the S-wave as

$$t_s = \frac{d_s}{\beta_0} = \frac{\sqrt{(x_s - x_0)^2 + z_0^2}}{\beta_0}, \tag{2}$$

where d_p and d_s, are the P- and S-wave distances, α_0 and β_0 are the true P- and S-wave speeds, and the distance between two receivers is $b = x_p - x_s$.

The horizontally extended SICP imaging condition, given in Shabelansky et al. (2015), for a single source is:

$$I(x_0, h_x, z) = \int_T^0 \underline{u}_p(x_0 + h_x, z, t) \cdot \underline{u}_s(x_0 - h_x, z, t) dt, \tag{3}$$

where $I(x_0, h_x, z)$ is the horizontally extended image (i.e., common image gather), and $\underline{u}_p$ and $\underline{u}_s$ are the displacement (vector) wavefields.

To mimic the kinematics of the extended imaging condition in equation 3, we analyze the interference of the wavefields in the horizontal space-lag extended image point (gather) by shifting the S-wave by h_x to the left (i.e., $-h_x$) and the P-wave by h_x to the right (i.e., $+h_x$) and keeping the same propagation travel times as those given in equations 1 and 2 (see Figure 2(a)). We

DOI http://dx.doi.org/10.1190/segam2015-5848434.1

compute the travel times for the migration wave speeds, α_1 and β_1, so for the P-wave travel time, we obtain,

$$t_p = \frac{\sqrt{(x_s+b-x_0-h_x)^2+z^2}}{\alpha_1}, \quad (4)$$

and for the S-wave,

$$t_s = \frac{\sqrt{(x_s-x_0+h_x)^2+z^2}}{\beta_1}. \quad (5)$$

Note that $z = z_0 \pm \delta z$ where δz is defined within the bars in Figure 2(a).

Then, we enforce that these travel times are equal to the recorded times. For the P-wave, we equate equations 1 and 4, and obtain:

$$(x_s+b-x_0)^2+z_0^2 = \left(\frac{\alpha_0}{\alpha_1}\right)^2\left[(x_s+b-x_0-h_x)^2+z^2\right], \quad (6)$$

or

$$(x_s-x_0)^2+z_0^2 = \left(\frac{\alpha_0}{\alpha_1}\right)^2\left[(x_s+b-x_0-h_x)^2+z^2\right] - 2(x_s-x_0)b-b^2, \quad (7)$$

and by equating equations 2 and 5 for the S-wave, we obtain:

$$(x_s-x_0)^2+z_0^2 = \left(\frac{\beta_0}{\beta_1}\right)^2\left[(x_s-x_0+h_x)^2+z^2\right]. \quad (8)$$

Next, we equate the left hand-sides of equations 7 and 8, and rearrange to obtain:

$$z(h_x) = z = \pm\sqrt{\frac{\left(\frac{\beta_0}{\beta_1}\right)^2(x_s-x_0+h_x)^2-\left(\frac{\alpha_0}{\alpha_1}\right)^2(x_s+b-x_0-h_x)^2+2(x_s-x_0)b+b^2}{\left(\frac{\alpha_0}{\alpha_1}\right)^2-\left(\frac{\beta_0}{\beta_1}\right)^2}}. \quad (9)$$

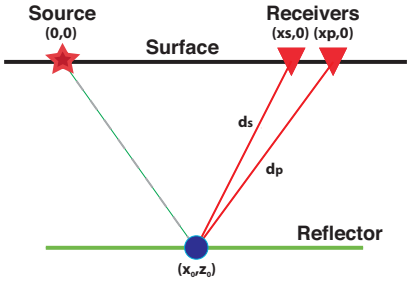

Figure 1: The path of the interfering P- and S-waves from a conversion point in the subsurface with two receivers at the surface.

The same procedure is applied for analyzing the inference when we shift the S-wave by h_x to the right (i.e., $+h_x$) and the P-wave by h_x to the left (i.e., $-h_x$) (see Figure 2(b)). The final equation for this case is obtained by replacing h_x with $-h_x$ in equation 9.

Equation 9 shows how the depth, z, of the moveout changes as a function of the horizontal space lag, h_x, for fixed ratios between the true and migration P- and S-wave speeds, α_0/α_1 and β_0/β_1, the subsurface horizontal position x_0, the surface position of the S-wave receiver, x_s, and its distance to the P-wave receiver, b. Note that z here does not behave hyperbolically as in standard WEMVA (e.g., Sava and Fomel, 2006; Mulder, 2014). Note also that the equation 9 is not well defined when the denominator is zero (i.e., $(\alpha_0/\alpha_1)^2-(\beta_0/\beta_1)^2=0$) and z may become complex for certain values of $(\alpha_0/\alpha_1)^2$ and $(\beta_0/\beta_1)^2$. Note however, that this is a limitation of the analytical derivation and not of the image construction in the extended domain, as will be shown below with the numerical results.

We are calculating the travel times of the interference and its corresponding depth, which implicitly makes a high frequency

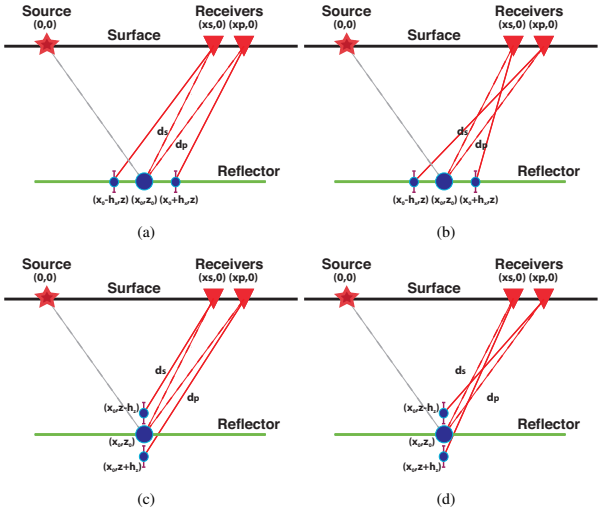

Figure 2: The paths of the interfering P- and S-waves for the extended space-lag imaging condition: (a) horizontally shifting P-wave to x_0+h_x and S-wave to x_0-h_x, (b) horizontally shifting P-wave to x_0-h_x and S-wave to x_0+h_x, (c) vertically shifting P-wave to $z+h_z$ and S-wave to $z-h_z$, and (d) vertically shifting P-wave to $z-h_z$ and S-wave to $z+h_z$. The bars at the points (x_0-h_x,z), (x_0+h_x,z), $(x_0,z-h_z)$ and $(x,z+h_z)$ indicate that the interference is depth dependent.

DOI http://dx.doi.org/10.1190/segam2015-5848434.1

assumption, in which the travel times appear in the phase term of the integral in equation 3. To determine the location of the receiver at which we would see the dominant contribution, we apply the method of stationary phase to solve for b, i.e. we compute

$$\frac{dz}{db} = 0, \tag{10}$$

and obtain

$$b = \frac{\left(\left(\frac{\alpha_0}{\alpha_1}\right)^2 - 1\right)(x_0 - x_s) \pm \left(\frac{\alpha_0}{\alpha_1}\right)^2 h_x}{\left(\left(\frac{\alpha_0}{\alpha_1}\right)^2 - 1\right)}. \tag{11}$$

By inserting b from equation 11 into equation 9, we remove the dependence of z on b.

Results

To show the behavior of the moveout, $z(h_x)$, in equation 9, we plot them in Figure 3 for a fixed $x_0 = 2000\ m$ and $x_s = 4000\ m$, and for varying P- and S-wave speed ratios. Three main observations can be deduced from this Figure. First, different P-wave speed perturbations correspond to different moveout slopes (see for example Figure 3(a)). Second, different S-wave speed perturbations correspond to different intercepts of the moveouts at $h_x = 0$ (n.b. the intercept in Figure 3(b) should be negative however is not defined because the moveout at negative $z(h_x = 0)$ is complex/imaginary). These two observations suggest that S-wave perturbation is more sensitive to vertical effects whereas the variations in the P-wave speed are more prone to horizontal effects. Physically, this may be explained by the fact that the travel path of the S-wave is more vertical than that of the P-wave (see Figure 1). The third observation is that when the denominator of equation 9 changes sign, the behavior of the moveout could become very complicated (see how the slopes and intercepts vary in Figures 3(c) and 3(d)).

To understand the behavior of the analytical moveouts in the horizontally extended domain, we numerically calculate the extended image gathers (Figure 4) using a 2D finite-difference pseudo-spectral solver and SICP imaging condition (Shabelansky, 2015, app. A and chap. 2). We calculate these extended images with correct and incorrect P- and S-wave speeds, as shown in the legends and caption of Figures 3 and 4, respectively. In Figure 4, we show these image gathers calculated for a single horizontal layer at the depth of 1 km. Note that the analytical moveouts in Figure 3 correspond to numerical moveouts in Figure 4 below 1 km depth. Note also that the analytical and numerical moveouts are slightly off because the numerical results were calculated with smoothed P- and S-wave speeds in order to prevent artificial/numerical artifacts. Three main observations are deduced from the comparison between Figures 3 and 4. First, we observe that the energy in Figure 4 moves along $h_x = 0$ with the perturbation of the background P- and S-wave speeds so the sensitivity to the wave speed errors is very high around the intercept (i.e., $h_x = 0$). We also observe the weak spread of the energy outside of $h_x = 0$ as a function P-wave speed perturbation, as predicted by the analytical moveouts (Figure 3). Second, even with the correct wave speeds (Figure 4(a)), we observe defocusing, as predicted in Figure 3(a) (see the red curve that describes best the moveout with the correct wave speeds; n.b., when the P- and S-wave speed ratios are equal, the analytical moveout is not well defined). Note however that in practice this defocusing, with the correct wave speeds, is typically suppressed by interfaces located above and below the target interface. The third observation is that the amplitude/wavelet of focusing signal is stretched for high P-wave speed ratios (slow migration P-wave speeds) or/and low S-wave speed ratios (high migration S-wave speeds) and squeezed conversely.

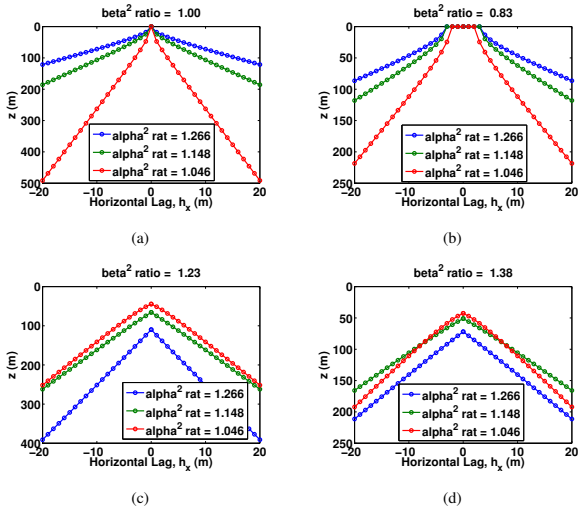

Figure 3: Analytical moveouts for SICP-WEMVA of $z(h_x)$ for a single interface with squared ratios between true and perturbed P- and S-wave speeds, shown above at each result.

Because we observed in Figure 3 that the slopes of the moveouts along h_x are sensitive to the perturbations in P-wave speed and the intercepts to the S-wave speed, and in Figure 4 most of the interference energy varies around $h_x = 0$, we derive and calculate the analytical moveouts and compute the numerical image gathers along the vertical space lags (i.e., h_z). Note that our primary goal is to investigate the dependence of the moveouts on P- and S-wave speed variations and to separate them into different domains so that the objective function of the SICP-WEMVA will be more sensitive and the algorithm will converge faster.

Vertical subsurface space-lag image gather

The derivation of moveout $z(h_z)$ follows the same steps as those for $z(h_x)$ for the following vertically extended SICP imaging condition

$$I(x_0, z, h_z) = \int_T^0 \underline{u}_p(x_0, z + h_z, t) \cdot \underline{u}_s(x_0, z - h_z, t) dt, \tag{12}$$

where

$$z(h_z) = z_{1,2} = \frac{-B \pm \sqrt{B^2 - 4AC}}{2A} \tag{13}$$

with

$$A = \left(\frac{\alpha_0}{\alpha_1}\right)^2 - \left(\frac{\beta_0}{\beta_1}\right)^2, \tag{14}$$

$$B = \pm 2h_z \left(\left(\frac{\alpha_0}{\alpha_1}\right)^2 + \left(\frac{\beta_0}{\beta_1}\right)^2\right), \tag{15}$$

DOI http://dx.doi.org/10.1190/segam2015-5848434.1

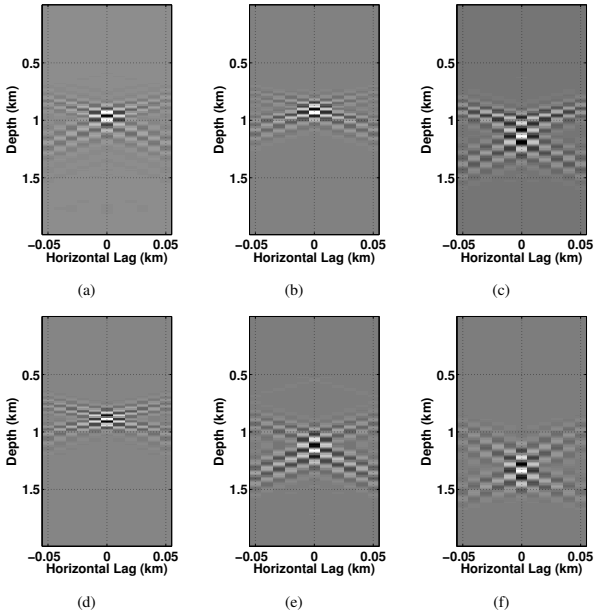

Figure 4: Extended horizontal subsurface space lag image gathers, $I(z,h_x)$, numerically calculated with P- and S-wave speeds $\left((\alpha_0/\alpha_1)^2,(\beta_0/\beta_1)^2\right)$: (a) (1,1), (b) $(0.83,1),(c)$(1.266,1), (d) $(1,1.23),(e)$(1,0.83), (f) (1.266,.0.84)

and

$$C = \left(\left(\frac{\alpha_0}{\alpha_1}\right)^2 - \left(\frac{\beta_0}{\beta_1}\right)^2\right)\left[(x_s - x_0)^2 + h_z^2\right] + \left(\left(\frac{\alpha_0}{\alpha_1}\right)^2 - 1\right)\left[2(x_s - x_0)b + b^2\right], \quad (16)$$

where for the stationary phase

$$b = -(x_s - x_0). \quad (17)$$

Note that $\pm$ in equation 15 corresponds to the positive and negative vertical shifts of the P- and S-wavefields (see Figures 2(c) and 2(d)).

By plotting the moveouts $z(h_z)$ (equation 13) in Figures 5 (a) and (b), we observe that the slope of the moveout is sensitive to variations in both P- and S-wave speeds and not only to the P-wave variation as was the case in Figure 3 with the moveouts along the horizontal subsurface space lags, h_x. The vertical moveouts calculated numerically in Figures 5 (c)-(e), with variations shown in the caption of this Figure, also demonstrate this observation. This behavior shows that the objective function will most likely be more sensitive to both wave speed variations, which may have significant implications on the resolution and convergence of the SICP-WEMVA for optimization of the background wave speeds. The numerical investigation of the resolution and convergence of SICP-WEMVA with objective functions and gradients from vertical extended images is the subject of future research.

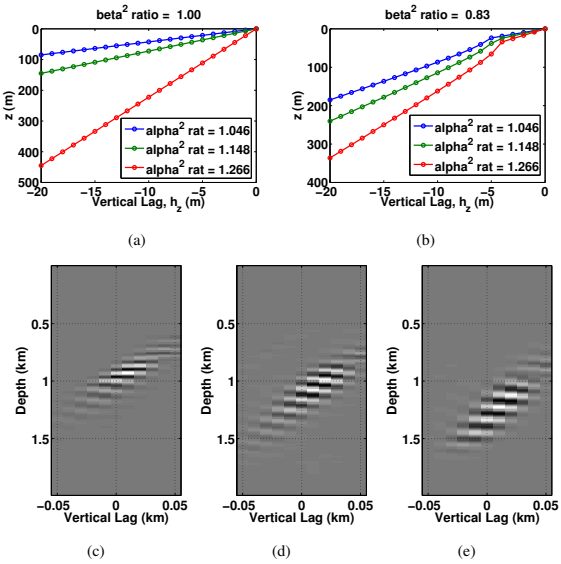

Figure 5: Analytical moveouts for SICP-WEMVA of $z(h_z)$ for a single interface. The squared ratios between true and perturbed P- and S-wave speeds (e.g., $(\alpha_0/\alpha_1)^2,(\beta_0/\beta_1)^2$), shown in the legends and titles in (a) and (b). Extended vertical subsurface space lag image gathers, $I(z,h_z)$, numerically calculated with P- and S-wave speeds $\left((\alpha_0/\alpha_1)^2,(\beta_0/\beta_1)^2\right)$: (c) (1,1), (d) (1,0.83), (e) (1.266,.0.83). Note that the slopes of the moveouts, both analytical and numerical, depend on variations in both P- and S-wave speeds.

CONCLUSIONS

In this study, we presented analytical derivations of the moveouts for SICP-WEMVA in the horizontal and vertical subsurface space-lag extended image domains. We compared the analytical and numerical moveouts and demonstrated that in the horizontally extended domain, the perturbations in P-wave speed correspond to different slopes and those in S-wave speed to different intercepts. However, in the vertically extended domain, the perturbations in both P and S-wave speeds affect the slopes. These observations suggest that we are able to separate the background wave speed perturbations into different extended image domains, and thus have significant implications on the accuracy and convergence of the SICP-WEMVA optimization.

ACKNOWLEDGMENTS

We thank ERL founding members consortium at MIT for funding this work. We also thank Yunyue Li and William L. Rodi for helpful discussion.

DOI http://dx.doi.org/10.1190/segam2015-5848434.1

EDITED REFERENCES

Note: This reference list is a copyedited version of the reference list submitted by the author. Reference lists for the 2015 SEG Technical Program Expanded Abstracts have been copyedited so that references provided with the online metadata for each paper will achieve a high degree of linking to cited sources that appear on the Web.

REFERENCES

Bostock, M., S. Rondenay, and J. Shragge, 2001, Multiparameter two-dimensional inversion of scattered teleseismic body waves 1. Theory for oblique incidence: Journal of Geophysical Research Solid Earth, **106**, B12, 30771–30782.

Brytic, V., M. V. de Hoop, and R. D. van der Hilst, 2012, Elastic-wave inverse scattering based on reverse time migration with active and passive source reflection data, *in* G. Uhlmann, ed., Inverse problems and applications: Inside out II: Mathematical Sciences Research Institute Publications, 411–453.

Esmersoy, C., 1990, Inversion of P and SV waves from multicomponent offset vertical seismic profiles: Geophysics, **55**, 39–50, http://dx.doi.org/10.1190/1.1442770.

Hardage, B. A., M. V. DeAngelo, P. E. Murray, and D. Sava, 2011, Multicomponent seismic technology: SEG, http://dx.doi.org/10.1190/1.9781560802891.

Mulder, W., 2014, Subsurface offset behaviour in velocity analysis with extended reflectivity images: Geophysical Prospecting, **62**, no. 1, 17–33, http://dx.doi.org/10.1111/1365-2478.12073.

Purnell, G. W., 1992, Imaging beneath a high-velocity layer using converted waves: Geophysics, **57**, 1444–1452, http://dx.doi.org/10.1190/1.1443212.

Rondenay, S., M. Bostock, and J. Shragge, 2001, Multiparameter two-dimensional inversion of scattered teleseismic body waves 3. Application to the Cascadia 1993 data set: Journal of Geophysical Research Solid Earth, **106**, B12, 30795–30807.

Sava, P., and S. Fomel, 2006, Time-shift imaging condition in seismic migration: Geophysics, **71**, no. 6, S209–S217, http://dx.doi.org/10.1190/1.2338824.

Shabelansky, A. H., 2015, Theory and application of source independent full wavefield elastic converted phase seismic imaging and velocity analysis: Ph.D. dissertation, Massachusetts Institute of Technology.

Shabelansky, A. H., A. Malcolm, S. Fehler, and M. Bakku, 2012, Seismic imaging of hydraulically-stimulated fractures: A numerical study of the effect of the source mechanism: 82nd Annual International Meeting, SEG, Expanded Abstracts, doi:10.1190/segam2012-1182.1.

Shabelansky, A. H., A. Malcolm, M. Fehler, and W. Rodi, 2014, Migration-based seismic trace interpolation of sparse converted phase micro-seismic data: 84th Annual International Meeting, SEG, Expanded Abstracts, 3642–3647.

Shabelansky, A. H., A. Malcolm, M. Fehler, X. Shang, and W. Rodi, 2013, Converted phase elastic migration velocity analysis: 83rd Annual International Meeting, SEG, Expanded Abstracts, 4732–4737.

Shabelansky, A. H., A. E. Malcolm, M. C. Fehler, X. Shang, and W. L. Rodi, 2015, Source-independent full wavefield converted-phase elastic migration velocity analysis: Geophysical Journal International, **200**, no. 2, 952–966, http://dx.doi.org/10.1093/gji/ggu450.

Shang, X., M. de Hoop, and R. van der Hilst, 2012, Beyond receiver functions: Passive source reverse time migration and inverse scattering of converted waves: Geophysical Research Letters, **39**, no. 15, http://dx.doi.org/10.1029/2012GL052289.

Stewart, R. R., 1991, Rapid map and inversion of P-SV waves: Geophysics, **56**, 859–862, http://dx.doi.org/10.1190/1.1443103.

Stewart, R. R., J. E. Gaiser, R. J. Brown, and D. C. Lawton, 2003, Converted-wave seismic exploration: Applied Geophysics, **68**, no. 1, 40–57, http://dx.doi.org/10.1190/1.1543193.

Vinnik, L., 1977, Detection of waves converted from P to SV in the mantle: Physics of the Earth and Planetary Interiors, **15**, no. 1, 39–45, http://dx.doi.org/10.1016/0031-9201(77)90008-5.

Vinnik, L., R. Avetisjan, and N. Mikhailova, 1983, Heterogeneities in the mantle transition zone from observations of P-to-SV converted waves: Physics of the Earth and Planetary Interiors, **33**, no. 3, 149–163, http://dx.doi.org/10.1016/0031-9201(83)90117-6.

Xiao, X., and W. Leaney, 2010, Local vertical seismic profiling (VSP) elastic reverse-time migration and migration resolution: Salt-flank imaging with transmitted P-to-S waves: Geophysics, **75**, no. 2, S35–S49, http://dx.doi.org/10.1190/1.3309460.